

Pd Ion-Exchange and Ammonia Etching of a Prussian Blue Analogue to Produce a High-Performance Water-Splitting Catalyst

Hao Zhang, Qianfan Jiang, Joseph H. L. Hadden, Fang Xie, and D. Jason Riley*

The authors report an ammonia-assisted in situ cation-exchange method for the synthesis of dodecagon N-doped PdCoNi carbon-based nanosheets (Pd-e-NiCo-PBA-C) and explore the catalytic performance. Pd-e-NiCo-PBA-C exerts extremely low overpotential and Tafel slope for hydrogen evolution reaction (HER) and oxygen evolution reaction (OER) both in acidic and alkaline media, only 47 mV, 55 mV dec⁻¹ (pH = 0, HER) and 147 mV, 67 mV dec⁻¹ (pH = 14, HER), and 309 mV, 67 mV dec⁻¹ (pH = 14, OER), outperforming commercial IrO₂-based and Pt-based catalysts. In addition, after 5000 cycles, the linear sweep voltammetry curve shows a negligible shift, indicating excellent stability performance. To test its overall water-splitting performance, Pd-e-NiCo-PBA-C is applied as both cathode and anode materials. A high current density of 33 mA cm⁻² at a battery voltage of 1.6 V is obtained, with the catalytic activity maintained at 97.3% after over 50 h. To get a further insight into the superior OER and HER performance, theoretical calculations are carried out, the better performance originates from the affinity difference of Pd and Ni atoms for gas atoms, and the replacement of inert atoms can decrease the binding energy and enhance the electrocatalytic activity.

1. Introduction

With increasing consumption of fossil fuels, coupled with the depletion of natural resources, there is an urgent need to develop sustainable energy conversion and storage devices, such as regenerative fuel cells, rechargeable metal–air batteries, and supercapacitors.^[1,2] These devices can generate and recycle energy to meet the demand of human society and decrease environmental pollution. Among the available renewable energy fuels, hydrogen (H₂) is considered to be the ideal clean energy source of the future, it has a high-energy density and can be prepared cleanly from water.^[3–5]

The widespread use of H₂ is currently subject to two major technical bottlenecks: i) the kinetic and thermodynamic slow

anodic oxygen evolution reaction (OER); and ii) the scarcity and high cost of the precious metal catalysts such as platinum and ruthenium (IV) oxide.^[6–8] High-performance hydrogen evolution reaction (HER) and OER bi-electrocatalysts should provide fast electron transfer, a high-density of catalytic active sites, suitable Gibbs energy for adsorbing atomic hydrogen and oxygen at low cost and high sustainability.^[9–11]


The construction of microstructures in the light of architecture, chemical composition, and structural subunit is one of the most promising ways to solve the challenges.^[12–14] For instance, complex porous structures as electrocatalytic materials consisting of secondary subunits with highly exposed active sites on the surface are expected to maximize the electrocatalytic activity.^[15,16] Multishell hollow particles increase the volumetric energy density and prevent the side reaction between the electrode and the electrolyte due to

their optimized empty space.^[17,18] Layered structures can effectively improve the number of exposed active sites and decrease the surface energy of active nanomaterials.^[19] Ordered architectures, as adhesive-free film/array electrodes, provide good electrochemical reaction platforms for high-energy storage and effectively avoid particle aggregation that may lead to cycle life degradation.^[20]

Prussian blue analogues (PBAs, A_xM[M'(CN)₆]_{1-y}·□_y·nH₂O, where A = alkali metal, M, M' = transition metals, □ = M'(CN)₆ vacancy, 0 < x < 2, 0 < y < 1), offer facile routes for the preparation of unique microstructures owing to their inherently large interstitial sites, redox active metal ions and open framework structures.^[21] Due to the coordination environment of PBAs, the metals inside can be partly exchanged with other metals to allow adjustment of the spatial distance of metal sites and form novel metal compounds.^[22,23] Moreover, the tailorable properties of PBAs can be enhanced by acid or alkali etching to yield unique microstructures with high specific surface area and high crystallinity.^[24,25] Following that, on account of the coexistence of both organic and inorganic substances in the etched PBAs, high yield carbon materials with uniformly distributed metal-particles can be in situ produced by carbothermal method.^[26–28]

Palladium is considered to be the most effective candidate for replacing Pt-based electrocatalysts as it has similar lattice constants and crystal structures but is cheaper and more

H. Zhang, Q. Jiang, Dr. J. H. L. Hadden, Dr. F. Xie, Prof. D. J. Riley
Department of Materials and London Centre for Nanotechnology
Imperial College London
London SW7 2AZ, UK
E-mail: jason.riley@imperial.ac.uk

 The ORCID identification number(s) for the author(s) of this article can be found under <https://doi.org/10.1002/adfm.202008989>.

© 2020 The Authors. Advanced Functional Materials published by Wiley-VCH GmbH. This is an open access article under the terms of the Creative Commons Attribution License, which permits use, distribution and reproduction in any medium, provided the original work is properly cited.

DOI: 10.1002/adfm.202008989

abundant.^[29] Changing the local structure of the material, alloying Pd with foreign metals and/or supporting Pd on metal oxides, has a significant impact on the electronic structure of Pd and its catalytic activity.^[30–33] Libuda et al. reported a Pd catalyst supported on Fe₃O₄, it was shown that a thin layer of PdO_x was formed at the interface between the particle surface and substrate when the metal atom was initially oxidized. This strong interaction changed the electronic structure of the Pd and enhanced catalytic activity.^[34–37] However, there are no studies reporting methods for the generation of Pd-based intermetallic compound derived from PBAs.

Herein, inspired by the excellent electrocatalytic activity of PBA derivatives and Pd-based composites, we use a novel in situ ammonia-assisted ion-exchange method to synthesize nitrogen-doped dodecagon PdCoNi crystals on carbon-based nanosheets from a PBA precursor. The NiCo-PBA was chosen as the precursor owing to its large surface area and zeolite-type cavities. The Pd containing dodecagons were formed by ion-exchange using a palladium salt in an alkaline ammonia solution. The as-formed material was demonstrated to exhibit excellent HER and OER catalytic activity and durability in a wide pH range. The encapsulation of CoPd₂ nanoparticles in an N-doped graphite carbon matrix effectively prevents their corrosion and leads to over 50 h catalytic activity in terms of overall water decomposition, which is superior to other recently reported dual-function electrocatalysts.

The enhanced water electrocatalysis activity of the as-formed material is attributed to the unique dodecagon nanosheets prepared in the procedure are multicomponents in the composite: 1) the CoPd₂ nanoparticles provide abundant active sites, which serve as catalytic centers for the reaction; 2) the Ni, N codoping and defectives produced in annealing effectively modulate the electronic configuration and optimizes the physicochemical properties; 3) the conductive graphite carbon matrix with large specific surface area as well as super-hydrophilic property can highly fasten the transportation of electrons and ions and facilitates electrolyte diffusion; 4) the unique dodecagon nanosheet structure exposes interfacial boundaries with different crystal surfaces and renders a shared conduction of electrons and ions, thus shortening the pathway of charged species and greatly enhancing water-splitting performance.

2. Experimental Section

2.1. Materials and Methods

2.1.1. Materials

Chemicals were analytical grade and obtained as follows: Nickel nitrate hexahydrate (≥98.5%), sodium citrate dihydrate (≥99.0%), potassium hexacyanocobaltate(III) (>99.0%), ammonia hydroxide (NH₃·H₂O, 28–30%), and palladium acetylacetonate (99.0%) were bought from Sigma-Aldrich. Absolute ethanol was purchased from VWR. They were used as received without further processing. Compressed argon gas was purchased from BOC. Reverse osmosis water (>18.2 MOhms cm⁻¹) was utilized in all experimental procedures.

2.1.2. Preparation of NiCo-Prussian Blue Analogue (NiCo-PBA)

Solution A was prepared by dissolving 0.6 mmol nickel nitrate and 0.9 mmol sodium citrate in 25 mL deionized water. Solution B was prepared by dissolving 0.4 mmol of potassium hexacyanocobaltate(III) in 25 mL of deionized water. Then, solution B was added to solution A dropwise under magnetic stirring over 10 min. The resultant solution was aged for 24 h at room temperature. The blue powdery product was collected by centrifugation, washed several times with deionized water, and vacuum dried at 60 °C overnight.

2.1.3. Preparation of Etched-NiCo-Prussian Blue Analogue (e-NiCo-PBA)

60 mg of the NiCo-PBA was dispersed in 30 mL of ethanol under ultrasonic agitation. Then, 30 mL of deionized water containing 7.5 mL of concentrated ammonia (28%) was added to the solution and the mixture was stirred for 1 h at room temperature. The light-blue powdery product was collected by centrifugation, washed several times with deionized water, and vacuum dried at 60 °C overnight.

2.1.4. Preparation of Pd-Etched-NiCo-Prussian Blue Analogue (Pd-e-NiCo-PBA)

60 mg of the NiCo-PBA was dispersed in 30 mL 10 mM palladium acetylacetonate ethanol solution with the assistance of ultrasound. Then, 30 mL of deionized water containing 7.5 mL of concentrated ammonia (28%) was added to the solution and it was stirred for 1 h at room temperature. The light-yellow powdery product was collected by centrifugation, washed several times with deionized water, and vacuum dried at 60 °C overnight.

2.1.5. Preparation of Prussian Blue Analogue-Carbon Composites

NiCo-PBA, e-NiCo-PBA, and Pd-e-NiCo-PBA powders were placed in ceramic boats and put in a tube furnace. The samples were heated to 350 °C with a heating rate of 1 °C min⁻¹, kept at 350 °C for 3 h under flowing argon gas, and then cooled at a rate of 10 °C min⁻¹ to room temperature. The obtained materials NiCo-PBA-C, e-NiCo-PBA-C, and Pd-e-NiCo-PBA-C were used without further treatment.

2.2. Characterization

Powder X-ray diffraction (XRD) patterns were collected on a Bruker D8 ADVANCE diffractometer with Cu K_α radiation (λ = 1.5418 Å). The structure and morphology of the samples were characterized by scanning electron microscopy (SEM, Hitachi S-4800) and transmission electron microscopy (TEM, JEOL-2100Plus). Energy-dispersive X-ray spectroscopy (EDS) attached to the SEM was used to analyze the composition of the nanoscale samples. The thermogravimetric analysis (TGA)

was conducted by using a Shimadzu-60 thermoanalyzer under a nitrogen and air flow with a heating rate of 10 °C min⁻¹ from room temperature to 600 °C, respectively. The N₂ adsorption–desorption isotherm were measured at 77 K using a Quantachrome Instruments Autosorb AS-6B. The samples were degassed in N₂ at 200 °C for 16 h prior to the measurements. The specific surface area was determined by the multipoint Brunauer–Emmett–Teller (BET) method and the pore-size distribution was calculated based on the Barrett–Joyner–Halenda (BJH) method. X-ray photoelectron spectroscopy (XPS) analysis was conducted on a PHI-5000 VersaProbe X-ray photoelectron spectrometer using an Al K α X-ray source.

2.3. Electrochemical Measurements

The electrochemical tests of the catalysts were performed using a Metrohm Autolab electrochemical workstation PGStat-12 (Utrecht, the Netherlands) connected to a three-electrode cell. A glassy carbon disk of 3 mm diameter served as the substrate for the working electrode for HER and OER studies. A Pt wire and saturated Ag/AgCl/Cl⁻ were employed as the counter electrode and reference electrode, respectively. An O₂-purged aqueous solution of 1 M KOH was the electrolyte for OER experiments and 0.5 M H₂SO₄ or 1 M KOH for HER studies. The catalyst (5 mg) was dispersed in 950 μ L of water/isopropanol solution (1:3) and 50 μ L Nafion (5%). The resulting solution was sonicated for 0.5–1 h. When the solution was well dispersed, 4 μ L of the above solution was dropped onto the clean glassy carbon electrode (GCE) for OER and HER studies giving a catalyst loading of 0.28 mg cm⁻². In order to ensure the H₂O/O₂ equilibrium, the system was tested at 1.23 V versus reversible hydrogen electrode (RHE) at room temperature in an electrolyte saturated with O₂.

Cyclic voltammetry (CV) curves were recorded at a sweep rate of 100 mV s⁻¹ for multiple cycles. Linear sweep voltammetry (LSV) was carried out at a scan rate of 5 mV s⁻¹ for polarization curves. LSV was performed several times until the signals were stabilized. CV curves with different scan rates (2, 4, 6, 8, and 10 mV s⁻¹) were measured over a potential range in which redox processes were absent to calculate the electrochemical double-layer capacitance: $C_{dl} = I_c/\nu$, where C_{dl} , I_c , and ν were the double-layer capacitance (F cm⁻²) of the electroactive materials, charging current (mA cm⁻²), and scan rate (mV s⁻¹). Electrochemical impedance spectroscopy (EIS) was measured by applying an AC voltage of 5 mV amplitude in a frequency range from 0.01 Hz to 100 kHz at the open circuit potential. All results reported in this work were converted to the RHE scale according to the Nernst equation without any iR-correction, where $E_{Ag/AgCl/Cl^-}$ was the working potential, and $E^0_{Ag/AgCl/Cl^-}$ equaled to 0.1976 V at 25 °C.

$$E_{RHE} = E_{Ag/AgCl/Cl^-} + 0.059 \times \text{pH} + E^0_{Ag/AgCl/Cl^-} \quad (1)$$

A self-made water-splitting device with a two-electrode configuration was assembled. Both the cathode and the anode electrodes were made by depositing Pd-e-NiCo-PBA-C onto Nickel foam (1 \times 1 cm²) and then drying in air. In order to obtain a total catalyst loading of about 1 mg cm⁻², the depo-

sition process was repeated several times. Then, the Nickel foam loaded with catalysts was fixed as an electrode, and it was installed on both sides of an “H” tube each component containing 1 M KOH solution separated by a Nafion membrane.

2.4. Theoretical Models

Calculations were performed with the QUANTUM ESPRESSO package (QE 6.5).^[38,39] Pseudopotentials of used atoms (Pd, Ni, Co, O, H, and C) were all taken from a standard solid-state pseudopotentials library.^[40] The plane-wave cutoff energy was set to 480 eV, the geometry optimization threshold was set to 1 \times 10⁻¹² N for force, and the convergence threshold for self-consistency was set to 1 \times 10⁻⁶ Ry. A slab unit cell with $a = b = 9.84$ angstrom was built, and c was set to 20 angstroms to prevent any interaction between layers.

3. Result and Discussion

3.1. Materials Characterization and Mechanism Explanation

The preparation of dodecagon carbon-based CoPd₂ nanosheets is achieved by applying in situ cation-exchange process of palladium with nickel assisted by ammonia etching, as shown in **Figure 1**. In the procedure, the precursor NiCo-PBA was reacted with ammonia and palladium acetylacetonate, and nickel ions were exchanged with palladium ions. At the same time, small nanoparticles aggregated to form Pd-e-NiCo-PBA with a dodecagon structure.

Monocrystalline NiCo-PBA was synthesized by a kinetically controlled crystallization method. **Figure S1a**, Supporting Information, compares the XRD patterns of the three precursors, NiCo-PBA, e-NiCo-PBA, and Pd-e-NiCo-PBA. On basis of the PBA crystal structure, the XRD of NiCo-PBA (Ni₃[Co(CN)₆]₂·12H₂O) was simulated by Pawley refinement method (**Figure 2a**). The diffraction peaks of the experimental and simulated XRD patterns match, the difference is negligible, which indicates good agreement between the experiment and simulation, confirming the product is of high purity and good crystallinity with a face-centered cubic structure. The microstructure of the prepared NiCo-PBA nanoparticles was characterized by field-emission scanning electron microscopy (FESEM). From **Figure 3a,b**, it can be seen the as-synthesized NiCo-PBA nanoparticles are of cubic morphology with relatively smooth surfaces and a uniform size of \approx 250–300 nm. Each vertex is truncated.

After the adding of an appropriate amount of ammonia and stirring for 1 h, the solid nanocubes can be converted into monocrystalline hollow nanocages. The XRD pattern of the material is almost identical to that of NiCo-PBA, only with a slight shift to higher angle (**Figure S1a**, Supporting Information), indicating a decrease in the water of crystallization. The as-obtained e-NiCo-PBA is a class of hollow nanostructure with cavities at each vertex of the cube-shaped nanoparticles (**Figure 3c–e**), inheriting the dimension of the nanocube precursors. From TEM images (**Figure 3n**), the nanoparticles are highly uniform; in agreement with the FESEM findings. The

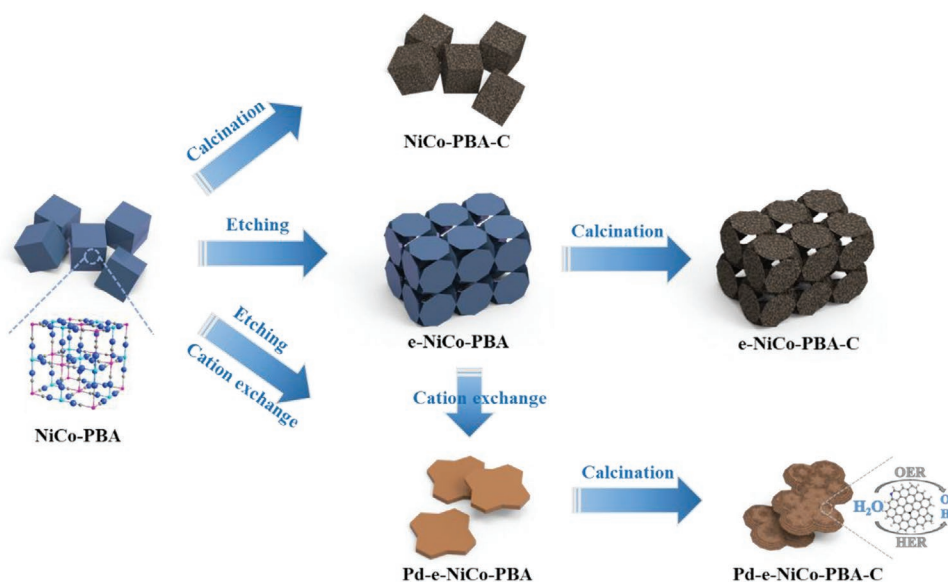


Figure 1. Schematic diagram of the synthesis of Pd-e-NiCo-PBA-C for highly efficient overall water splitting.

cubic nanocage is a monolith formed by the support of six nanodisks, each of which acts as a cage wall, attached adjacent to each other to form a 3D structure. In addition, the asymmetrical inner and outer surface structure can be seen from the TEM image. The outer surface is flat and the inner surface is pyramidal. The center thickness of these walls is ≈ 60 nm and the side is ≈ 30 nm.

Unlike other cubic hollow nanostructures, the nanoframe structure is the result of selective chemical etching with ammonia, which starts from the smooth apex angle along the precursor cubic structure. The extension is gradually transformed into a cage structure and eventually forms a hollow structure. It can be seen that the etching is along the $\langle 111 \rangle$ direction, and the $\{111\}$ faces were etched more quickly in ammonia than the $\{100\}$ faces, which indicates a dynamic etching process with the etching rate depending on the crystal surface. It has been previously reported that the flat surface of PBA has a higher stability than the corners or edges.^[12,13] Therefore, the eight corners of the cube can dissolve faster during the etching process, resulting in a nanoframe-like morphology.

To test this, time-dependent electron microscopy of a sample was performed to study the structural transformation process. Figure S2, Supporting Information, shows the morphology and structure of the intermediates. As the etching time increases, the morphology and structure of the precursor changes from a nanocube to a hollow nanocage, and finally to tapered nanosheets. First, after 30 min of etching, a slightly truncated structure can be seen at the eight apex angles of the nanocube, which has more defects and higher reactivity at the edges and apex angles than the faces (Figure S2a,b, Supporting Information). After treatment with aqueous ammonia for 1 h, the etching proceeds preferentially along the diagonal, and a distinct cavity begins to form at the vertex. Then, the etching cavity inside the nanocube becomes deeper and wider, and finally, the etched cavity of eight corners converges in the center of the nanocube to form a hollow cage-like nanostructure. After the reaction was carried out for 1.5 h, as shown in Figure S2c,d, Supporting Information, the eight apex angles of each nanocube were etched, while the six faces remained almost unchanged; one cube eventually split into six unique nanocone structures.

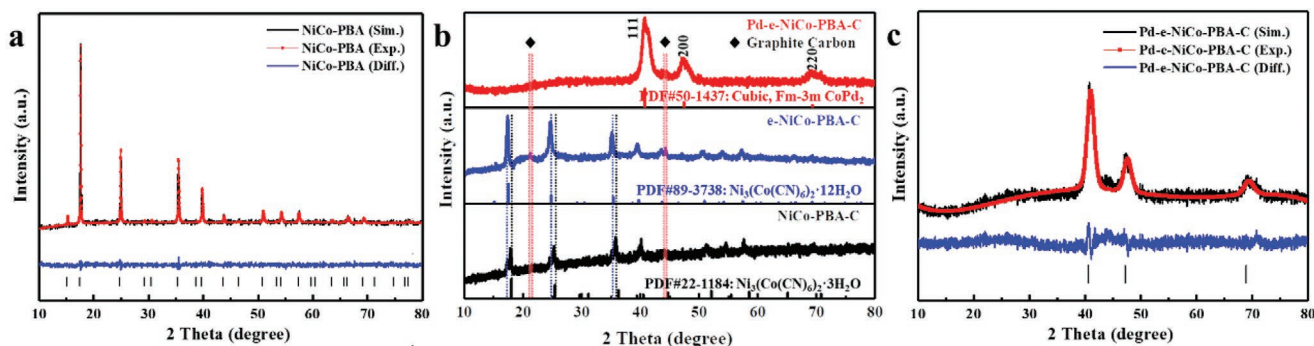


Figure 2. a) XRD refinement of $\text{Ni}_3(\text{Co}(\text{CN})_6)_2$ (NiCo-PBA). b) XRD patterns of Pd-e-NiCo-PBA-C, e-NiCo-PBA-C, and NiCo-PBA-C. c) XRD refinement of Pd-e-NiCo-PBA-C.

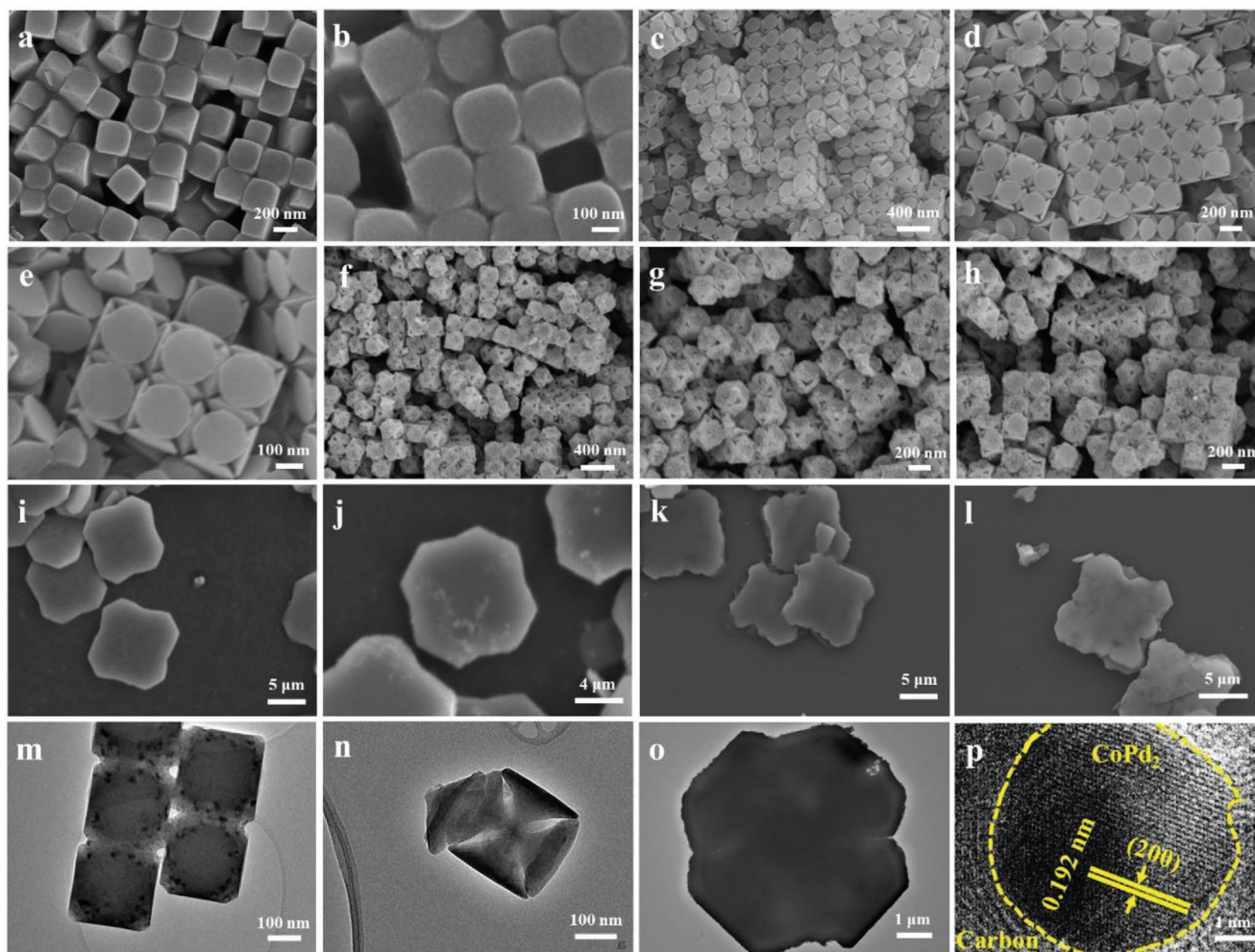


Figure 3. SEM images of a,b) NiCo-PBA, c–e) e-NiCo-PBA, f–h) e-NiCo-PBA-C, i,j) Pd-e-NiCo-PBA, and k,l) Pd-e-NiCo-PBA-C. TEM images of m) NiCo-PBA-C, n) e-NiCo-PBA-C, and o) Pd-e-NiCo-PBA-C. p) HRTEM images of Pd-e-NiCo-PBA-C.

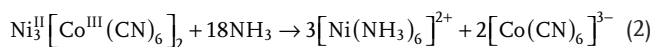
On addition of palladium acetylacetonate, due to the cation exchange between nickel ions and palladium ions, the nano-frames can be transformed into Pd-e-NiCo-PBA. The XRD pattern (Figure S1a, Supporting Information) reveals that the material is highly pure and crystalline. Figure 3i,j show SEM images with different magnifications of the as-synthesized dodecagon nanosheets; the diameter and thickness of the nanoplates are $\approx 10 \mu\text{m}$ and 10 nm, respectively.

SEM images (Figure S3, Supporting Information) show that with an increase in the amount of ammonia added, the structure of the as-formed nanosheets changes from a butterfly-shaped zigzag to dodecagon to nanoflower to a thinner nanoflower structure. This tendency could be masking the action of palladium acetylacetonate toward specific crystalline surfaces and impeding their oriented growth.^[41–43] The speed-determining step of ion exchange is the back-diffusion of ions in the solid, provided that the concentration of incoming ions on the surface is sufficiently high, and stirring does not allow excessive concentrations of effluent ions to accumulate on the surface of the exchanging material.^[44]

TGA was used to investigate the decomposition temperatures of NiCo-PBA and the e-NiCo-PBA (Figure 4a); it can be

seen that there are slight differences between the two samples when the temperature increased to 300 °C. The weight loss of 3.9% corresponds to the loss of one CN ligand per Co center in the material.^[45]

Figure 4b shows Fourier transform infrared (FTIR) spectra of the PBA precursors to investigate the chemical composition changes of the products at different OH^- etching reaction time. With an etching time from 0 to 1 h, it was observed that the $\nu(\text{CN})$ peak of $\text{Ni}^{\text{II}}-\text{N}\equiv\text{C}-\text{Co}^{\text{III}}$ at 2364 cm^{-1} relative to $\nu(\text{CN})$ peak of $\text{Ni}^{\text{II}}-\text{N}\equiv\text{I}-\text{Co}^{\text{II}}$ at 2182 cm^{-1} was significantly reduced, indicating that the ammonia mainly etched $\text{Ni}^{\text{II}}-\text{N}\equiv\text{C}-\text{Co}^{\text{III}}$, not $\text{Ni}^{\text{II}}-\text{N}\equiv\text{C}-\text{Co}^{\text{II}}$.^[46] In general, Co^{III} has a stronger affinity with the $-\text{CN}-$ group than Co^{II} , which means that the electron donating ability of the N atom in $-\text{N}\equiv\text{C}-\text{Co}^{\text{III}}$ is weaker than that of N atom in $-\text{N}\equiv\text{C}-\text{Co}^{\text{II}}$. Therefore, the bond between Ni^{II} and $-\text{N}\equiv\text{C}-\text{Co}^{\text{III}}$ is weaker and more easily destroyed than the bond between Ni^{II} and $-\text{N}\equiv\text{C}-\text{Co}^{\text{II}}$. According to this analysis, the following chemical reactions may occur during the etching process:



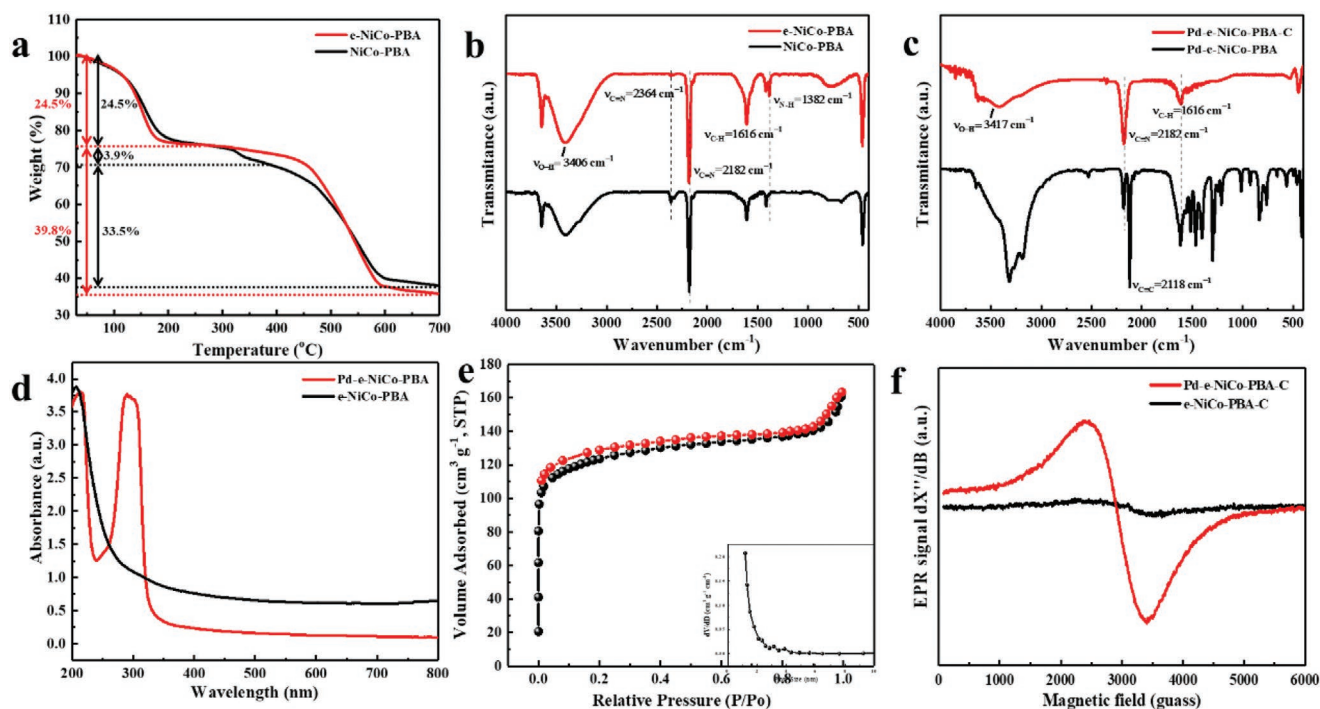
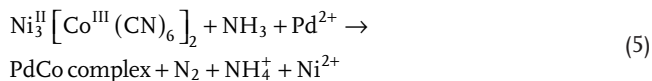
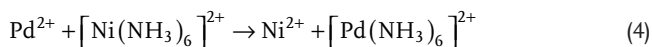
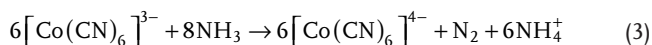


Figure 4. a) TGA of NiCo-PBA and e-NiCo-PBA. b) FTIR of NiCo-PBA and e-NiCo-PBA. c) FTIR of Pd-e-NiCo-PBA and Pd-e-NiCo-PBA-C. d) UV-Vis of e-NiCo-PBA and Pd-e-NiCo-PBA. e) BET (Inset: pore distribution) of Pd-e-NiCo-PBA-C. f) X band EPR spectra of e-NiCo-PBA-C and Pd-e-NiCo-PBA-C at room temperature.



It can be seen from the above equation that Ni^{2+} derived from $\text{Ni}^{\text{II}}-\text{N}\equiv\text{C}-\text{Co}^{\text{III}}$ can be stabilized by coordination with aqueous ammonia in the ligand exchange reaction (Equation (2)). In addition, the redox reaction occurred simultaneously in the etching process, and the $\nu(\text{NH})$ peak of NH_4^+ appeared at 1382 cm^{-1} in the FTIR spectrum after etching (Figure 4b), which supports a redox reaction occurring in the ammonia treatment process (Equation (3)).^[47]

The TEM and FTIR analysis indicates that $\text{Ni}^{\text{II}}-\text{N}\equiv\text{C}-\text{Co}^{\text{III}}$ and $\text{Ni}^{\text{II}}-\text{N}\equiv\text{C}-\text{Co}^{\text{II}}$ coexist in the nanocubes and distribute unevenly. $\text{Ni}^{\text{II}}-\text{N}\equiv\text{C}-\text{Co}^{\text{III}}$ are mainly distributed in the apex angle and center position of the nanocubes, while $\text{Ni}^{\text{II}}-\text{N}\equiv\text{C}-\text{Co}^{\text{II}}$ is located near the surface of the nanocubes.

EDS mapping (Figure 5a₁–e₁) confirms that the as-treated product contains C, N, O, Ni, Co, and Pd. The content of Ni is relatively low according to the signal intensity and elemental distribution. The cation concentrations of Co, Ni, and Pd in e-NiCo-PBA and Pd-e-NiCo-PBA are calculated from the results of inductively coupled plasma spectroscopy (ICP) measurement. Under the same feeding conditions, the results showed that the concentrations of Ni, Co, and Pd in e-NiCo-PBA were 0.950 ppm, 0.582, and 0.0002 ppm, respectively, and the

concentrations of these elements in Pd-NiCo-PBA were 0.192, 0.602, and 1.103 ppm. Therefore, the atomic percentages of Ni, Co, and Pd in these three elements are 59.84%, 40.14%, and 0.01%, while the atomic percentages of the elements in Pd-e-NiCo-PBA are 12.53%, 31.73%, and 58.14%, respectively. From these results, it is shown the percentage of Ni greatly decreases, and the percentage of Co decreases slightly, while the percentage of Pd increases sharply. Therefore, the cation exchange mainly occurs between Pd^{2+} and Ni^{2+} , with potentially a small amount of Pd^{2+} and Co^{2+} exchange.

NiCo-PBA, e-NiCo-PBA, and Pd-e-NiCo-PBA were calcined in nitrogen at a temperature of $350\text{ }^\circ\text{C}$ for 3 h. The XRD pattern (Figure 2b) reveals that the calcined product, Pd-e-NiCo-PBA-C, was composed of CoPd_2 (JCPDS no. 50-1437) and graphitic carbon. The peaks at $2\theta = 40.8^\circ$, 47.4° , and 69.3° corresponds to (111), (200), and (222) CoPd_2 planes, respectively. There are also two small peaks at about 21.4° and 44.3° , which can be attributed to (100) and (002) planes of graphite. The same graphite peaks also appear in the XRD pattern of e-NiCo-PBA-C, which indicates the graphitization of e-NiCo-PBA during the annealing process. For NiCo-PBA-C, there is only a broad peak around 22° , confirming the existence of amorphous carbon rather than graphitic carbon. The sintering products of nanocubes and nanoframes, NiCo-PBA-C and e-NiCo-PBA-C, maintain a similar crystal structure and composition as the precursors NiCo-PBA and e-NiCo-PBA, respectively; the differences are based on intensity and a slight peak shift. Compared with NiCo-PBA-C, e-NiCo-PBA-C has a larger full width at half maximum and a mildly low-angle shift, indicating it has smaller crystal size and retains more water of crystallization after calcination.

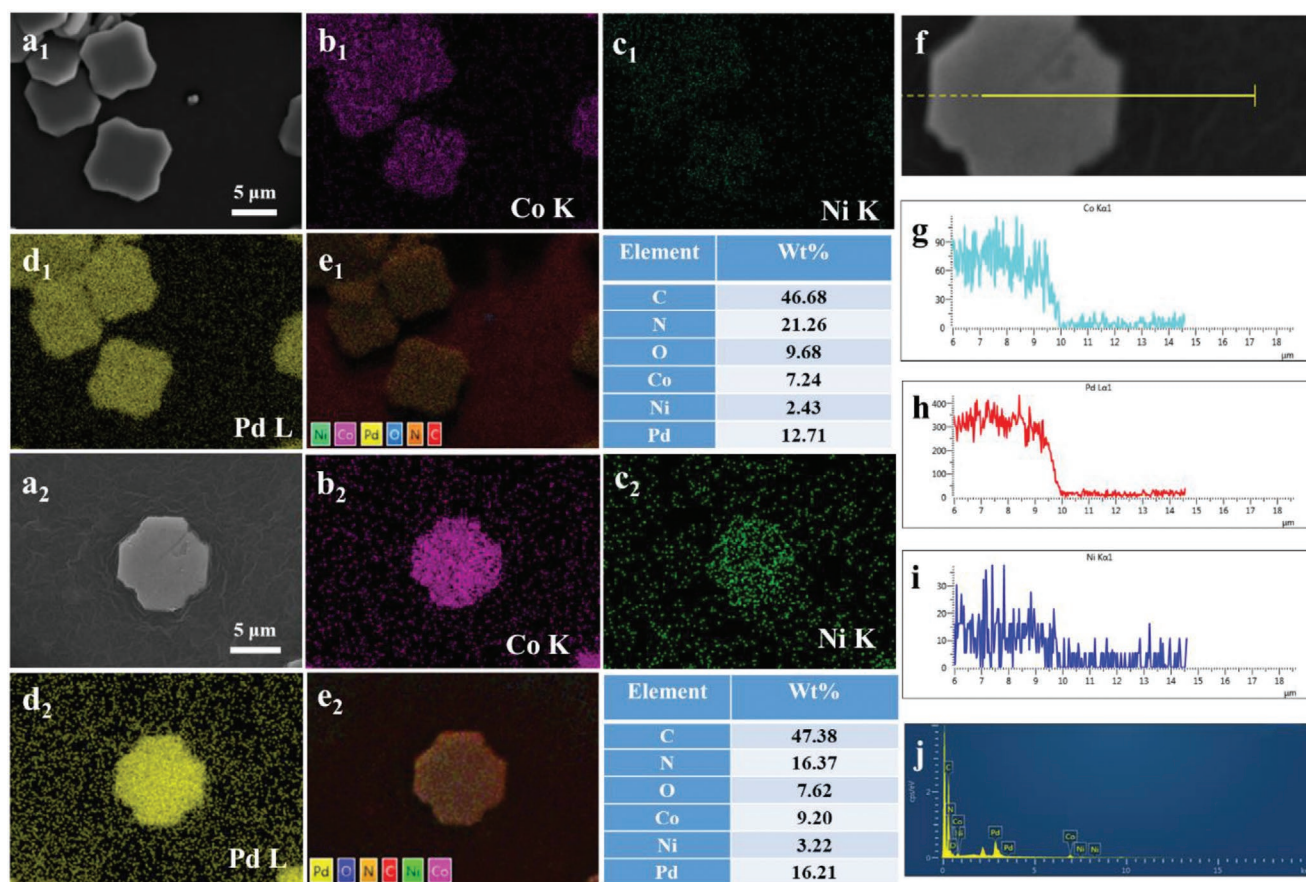


Figure 5. a₁) SEM images and b₁–e₁) mapping of Pd-e-NiCo-PBA. a₂) SEM images and b₂–e₂) mapping of Pd-e-NiCo-PBA-C. f–i) SEM line-scanning. j) EDS of Pd-e-NiCo-PBA-C.

It is worth mentioning that e-NiCo-PBA can also be transformed into the same dodecagon nanosheets of Pd-e-NiCo-PBA directly by reaction in palladium acetylacetonate solution containing ammonia, which confirms the initial morphology of the precursor has little effect on the reaction. Pd-e-NiCo-PBA can be calcinated to Pd-e-NiCo-PBA-C in argon, indicating carbon and cyanide ligand acts as reducing agents, converting the metal centers to lower oxidation states. The thermal reduction reaction of the CoPd₂ system is formed by the reaction of two cyanide-containing polymerization intermediates, CoPd(CN)₄ and Pd(CN)₂, which are formed upon reduction of Co³⁺ to Co²⁺ and involve a major rearrangement of the coordination structures. After further heating, these two intermediates are reduced to metal products, and these products form a single CoPd₂ composite product through solid-state diffusion.^[48]

SEM images (Figure 3k,l) show Pd-e-NiCo-PBA-C is of similar morphology to the original precursor Pd-e-NiCo-PBA, both are 2D dodecagon structures. Pd-e-NiCo-PBA-C has a rough surface, which make it an ideal catalytic electrode material because of both high crystallinity and a large accessible specific surface area. The TEM image (Figure 3o), shows the dodecagon nanosheets. The lattice fringes (Figure 3p and Figure S2h, Supporting Information) of 0.192, 0.135, 0.221 nm correspond to (200), (220), and (111) planes of CoPd₂, respectively, and

HRTEM image (Figure S2g, Supporting Information) also shows that CoPd₂ appears as a typical polycrystal structure.

ICP was conducted to determine the precise content of the metal elements in Pd-e-NiCo-PBA-C, the concentrations of Ni, Co, and Pd were 0.261, 0.864, and 1.339 ppm, combined with the EDS results (Figure 5), which suggests the weight percentages of Ni, Co, and Pd were 3.22%, 9.20%, and 16.21%, respectively, and thus it is concluded that there is a small number of Ni content in the catalyst. In the HRTEM there is no lattice distortion caused by Ni incorporation within the CoPd₂ nanoparticles. In addition for the XRD diffraction pattern of CoPd₂ in the as-formed material, there is no obvious peak shift compared with the simulated XRD patterns, from the XRD refinement result (Figure 2c), and the lattice parameter (a, b, c) is 3.8529 Å which is extremely close to the value of the reference pattern, 3.8296 Å (JCPDS no. 50–1437). These results suggest the remnant Ni content mainly exists in the carbon matrix and not the CoPd₂ nanoparticles.

UV–vis spectroscopy (Figure 4d) was also used to prove the doping of palladium into the nanostructure by preferential etching and ion exchange. After the addition of palladium acetylacetonate, peak appears around 293 nm in the UV–vis spectra, and the peak near 200 nm has a slight red shift, which suggests the existence of palladium ions.^[49,50] The color of the precursor solution changed from blue (NiCo-PBA) to

light-yellow (Pd-e-NiCo-PBA) gradually after stirring for about 10 min, which serves as macroscopic proof of the ion exchange.

The specific surface areas and pore structures of e-NiCo-PBA-C and Pd-e-NiCo-PBA-C were measured by nitrogen adsorption–desorption analysis (Figure 4e and Figure S5, Supporting Information). Adsorption–desorption curves of Pd-e-NiCo-PBA-C show a type I isotherm, indicating the existence of micropores. The specific surface areas were calculated by the BET method. Pd-e-NiCo-PBA-C has a BET surface area of 420.31 m² g⁻¹, which is larger than that of e-NiCo-PBA-C (56.15 m² g⁻¹). The pore volume of Pd-e-NiCo-PBA-C was raised from the 0.0369 cm³ g⁻¹ of e-NiCo-PBA-C to 0.1655 cm³ g⁻¹, demonstrating it has a larger specific surface area and abundant pore structures, thus improving contact area with electrolyte and electron transport efficiency, and hence is expected to exert better OER and HER performance. The pore-size distribution was calculated by the BJH method because of the existence of both micropores and mesopores. It revealed the sizes were centered at less than 1, 3.14, and 3.95 nm, which is consistent with mainly micropores and a few mesopores, corresponding to the result of type I isotherm curves.

Electron paramagnetic resonance (EPR) was conducted to study the effect of metal centers on the electronic properties of materials. It has been found that the incorporation of metal centers greatly alters the EPR signal, suggesting that free radical signals may make a difference in the electrochemical activity. It can be seen in Figure 4f that the introduction of Pd²⁺ greatly enhanced the radical signal. It resembles the signal of a carbon centered radical commonly found in amorphous carbon materials.

SEM and EDS mapping results of Pd-e-NiCo-PBA-C are displayed in Figure 5a₂–e₂,5j. C, N, O, Ni, Co, and Pd are still present, at similar ratios to the precursor before annealing. The percentages of Ni, Co, and Pd have slightly increased, while those of C, N, and O have slightly reduced. This loss of C, N, and O can be attributed to the matrix evaporation and carbonization during the sintering process. SEM line-scanning was also conducted to analyze longitudinal element distribution of the sample. The content of Co and Pd in Figure 5f–i is much greater than Ni, indicating the exchange of Ni²⁺ with Pd²⁺, which matches well with the previous characterization result.

The composition of Pd-e-NiCo-PBA-C is further supported by XPS. The survey scan spectrum indicates that nanosheets are composed of C, N, O, Ni, Co, and Pd elements (Figure 6). From the high-resolution XPS spectrum in Figure 6a, it can be seen that the fitted C 1s spectrum reveals a main peak at around 284.6 eV corresponding to C=C, and the peaks at 285.6 and 287.1 eV are assigned to C=N and C=O bonds, respectively. Notably, compared with the fitted C 1s spectrum of e-NiCo-PBA-C (Figure 6g and Figure S6b, Supporting Information), the slight shift of C=O bonds is due to the appearance of abundant oxygen vacancies and defects during the annealing process. The N 1s spectrum (Figure 6b) can be fitted into three peaks at 398.2, 398.9, and 400.5 eV, which correspond to pyridinic nitrogen, pyrrolic nitrogen, and quaternary nitrogen, respectively. The three nitrogen species have different adsorption capacities for water molecules; water molecules are more easily adsorbed on pyridinic nitrogen, then quaternary nitrogen, and poorly adsorbed pyrrolic nitrogen. During water electrocatalysis,

both pyridinic nitrogen and quaternary nitrogen can have better water wettability and larger contact areas, thus facilitating electron transfer in OER and HER.^[51] Compared with the XPS spectra of e-NiCo-PBA-C (Figure 6h and Figure S6b, Supporting Information), the relative content of pyridinic nitrogen and quaternary nitrogen of Pd-e-NiCo-PBA-C is much higher, indicating a potential better electrocatalysis performance. The O 1s peaks (Figure 6c) at 532.1 and 535.8 eV are assigned to metal–oxygen bonds (O1), oxygen ions in anoxic region (O2) and hydroxyl group (O4), respectively.^[52] For e-NiCo-PBA-C, the fitted O 1s peaks (Figure S6c, Supporting Information) can be split into two peaks, O1 and O4. The appearance of O2 in Pd-e-NiCo-PBA-C can be related to the dramatic increase in the oxygen vacancy concentration (*V_o*) caused by reduction of cyanide ligands during the annealing process. In addition, the Co 2p peaks (Figure 6d) of Pd-e-NiCo-PBA-C found at 775.2 and 797.6 eV can be assigned to 2p_{3/2} and 2p_{1/2} spins of Co⁴⁺, and the two peaks at 782.1 and 801.7 eV are attributed to 2p_{3/2} and 2p_{1/2} spins of Co³⁺, indicating the coexistence of Co³⁺ and Co⁴⁺ in Pd-e-NiCo-PBA-C. The relatively weak satellite peaks demonstrate the predominance of Co³⁺ in the near-surface region.^[53] The Ni 2p XPS spectrum (Figure 6e,i) is noisy compared with e-NiCo-PBA-C, which is due to the relatively low content of Ni. The two characteristic peaks at binding energies of 833.5 and 855.9 eV correspond to 2p_{3/2} and 2p_{1/2} spins of Ni²⁺, respectively. High resolution Pd 3d spectrum (Figure 6f) gives four deconvolution peaks at 338.4, 339.1, 343.9, and 344.3 eV, corresponding to Pd²⁺, Pd of 3d_{5/2} and Pd²⁺, and Pd of 3d_{3/2}, respectively, in Pd-e-NiCo-PBA-C.^[54]

3.2. Electrochemical Performance Evaluations

The electrocatalytic activities of Pd-e-NiCo-PBA-C for HER and OER in both 0.5 M H₂SO₄ and 1.0 M KOH electrolyte using a standard three-electrode system were investigated. Pd-e-NiCo-PBA-C was coated on a GCE, activated by CV at a scan rate of 10 mV s⁻¹ before the test, to ensure the measured electric current is attributable to HER and OER in the polarization curves rather than catalysts themselves.

After that, Pd-e-NiCo-PBA-C was coated on nickel foam to test the overall water-splitting performance, where the Pd-e-NiCo-PBA-C@Ni foam with dimensions of 1 × 1 cm² was used as both cathode and anode electrode and tested in a two-electrode system.

The HER performance of the samples was tested under acidic and alkaline conditions. The LSV curves are shown in Figure 7a. In 0.5 M H₂SO₄, the overpotential (*η*) values needed for Pd-e-NiCo-PBA-C treated electrodes to deliver 10 and 20 mA cm⁻² (i.e., *η*_{10HER-acidic}, *η*_{20HER-acidic}) are only 48 and 72 mV, respectively. Similarly, very small overpotential (i.e., *η*_{10HER-alkaline}, *η*_{20HER-alkaline}) of 147 and 182 mV are required in 1 M KOH to reach the same current densities (Figure 7b). In addition, the Tafel slopes (Figure 7d,e) of Pd-e-NiCo-PBA-C in acidic and alkaline solution are 55 and 67 mV dec⁻¹, respectively, which implies that chemical adsorption of H⁺ on the catalyst limits the reaction rate.^[49]

To investigate the structure–performance relationship of Pd-e-NiCo-PBA-C, comparative tests on different samples,

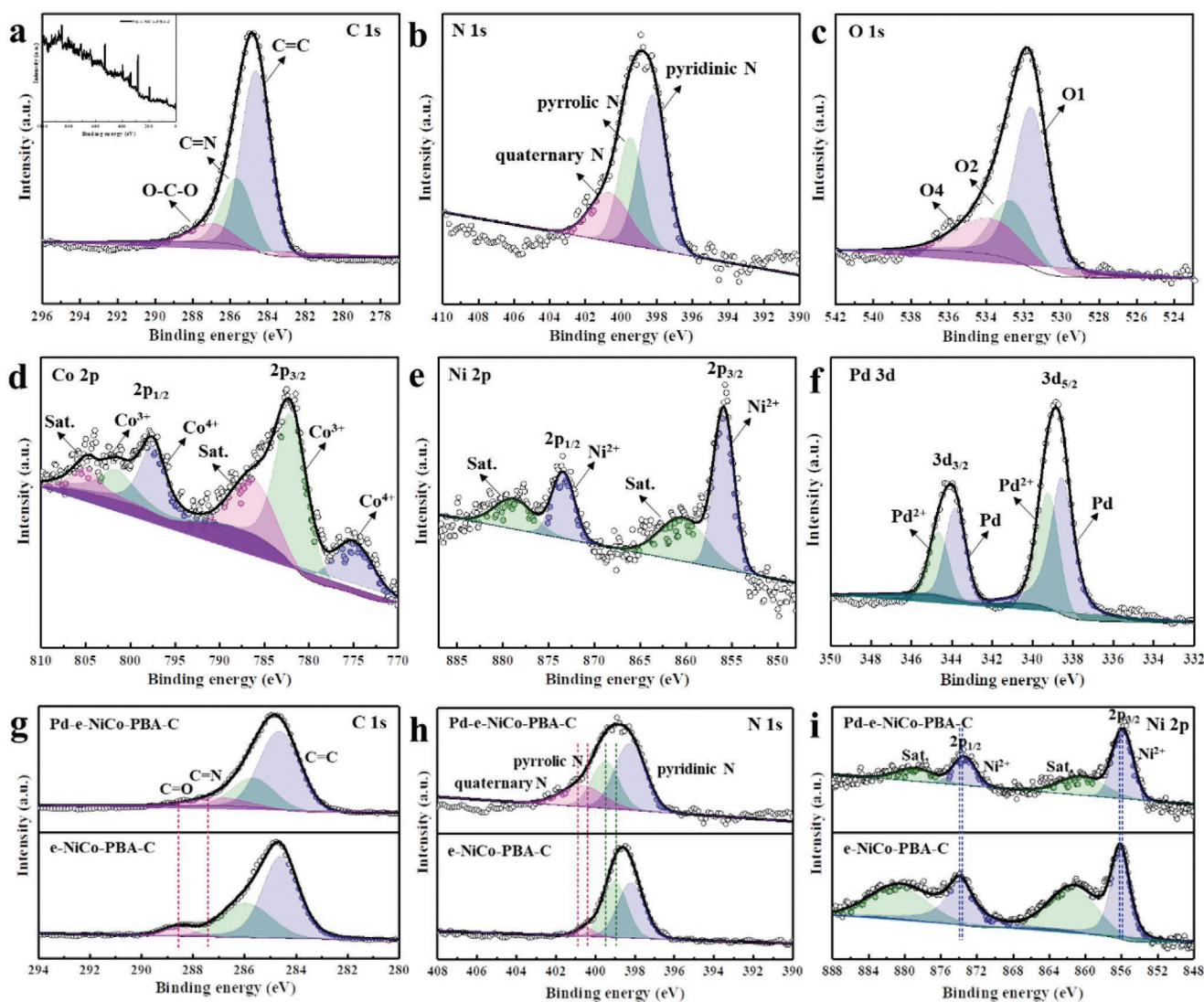


Figure 6. a) X-ray photoelectron spectroscopy (XPS) survey spectrum and high-resolution spectra at C 1s, b) N 1s, c) O 1s, d) Co 2p, e) Ni 2p, and f) Pd 3d regions of Pd-e-NiCo-PBA-C. XPS comparison spectrum at g) C 1s, h) N 1s, and i) Ni 2p of Pd-e-NiCo-PBA-C and e-NiCo-PBA-C. The spectra were shown with raw data and fitting data derived by Lorentz–Gaussian function.

including the annealed products, NiCo-PBA-C, e-NiCo-PBA-C, commercial Pt/C-10%, and a bare GCE were performed.^[55–57]

In acidic electrolyte, the overpotentials needed to deliver anodic current densities of 10 and 20 mA cm⁻² are compared in Figure 8a. The $\eta_{10\text{HER-acidic}}$, $\eta_{20\text{HER-acidic}}$ of NiCo-PBA-C, e-NiCo-PBA-C, and commercial Pt/C-10% are 575, 618; 632, 683; and 74 mV, 105 mV. Moreover, the Tafel slope comparison results of NiCo-PBA-C, e-NiCo-PBA-C and commercial Pt/C-10%, displayed in Figures 7d and 8b, were calculated to be 122, 128, and 82 mV dec⁻¹, respectively. It is noteworthy that the both overpotential and Tafel slope of Pd-e-NiCo-PBA-C are at a minimum among these catalysts, even lower than commercial Pt/C, corresponding to the best catalytic performance.

The HER performance comparison under alkaline conditions can be viewed in Figure 8a,b. It was found that NiCo-PBA-C, e-NiCo-PBA-C, and commercial Pt/C-10% all had higher overpotentials for reaching current densities of 10 and

20 mA cm⁻² ($\eta_{10\text{HER-alkaline}}$, $\eta_{20\text{HER-alkaline}}$), which were 472, 502; 583, 634; and 268 mV, 313 mV, respectively. The Tafel Slope (Figures 7e and 8b) of three samples were calculated as 102, 157, and 118 mV dec⁻¹, respectively. Tafel slope values in the range of 40–120 mV dec⁻¹ suggest the reaction on the surface follows the Volmer–Heyrovsky mechanism. The reasons for the difference of HER performance may be due to strength of bonding between different crystal planes and hydrogen as well as surface reconstruction caused by adsorption of hydrogen.^[49] The repeatability was also tested on Pd-e-NiCo-PBA-C and other references by fabricating six electrodes for each sample, and it was found that there was a small variation of <5% for experiments carried out either in 0.5 M H₂SO₄ or 1 M KOH (Figure S16, Supporting Information). In addition, Pd-e-NiCo-PBA-C catalysts also showed excellent HER stability in continuous tests, and the increase in overpotential was negligible after 5000 cycles (Figure 7h).

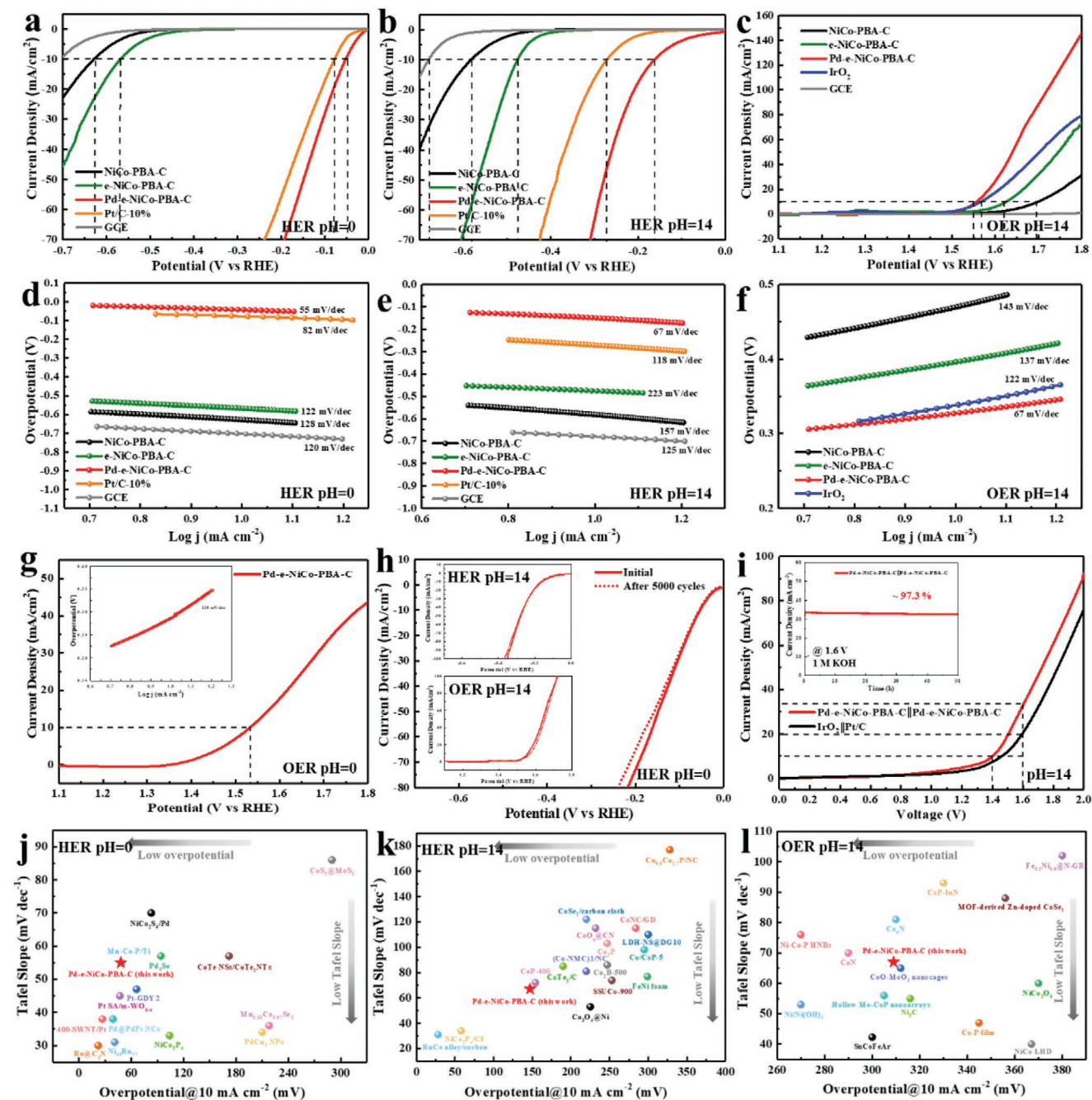


Figure 7. Electrochemical performance. a,b) Hydrogen evolution polarization curves of Pd-e-NiCo-PBA-C and the reference samples in 0.5 M H₂SO₄ solution (pH = 0) and 1.0 M KOH solution (pH = 14). c) Oxygen evolution polarization curves of Pd-e-NiCo-PBA-C and the reference samples in 1.0 M KOH solution (pH = 14). d,e) Hydrogen evolution Tafel plot of Pd-e-NiCo-PBA-C and the reference samples in 0.5 M H₂SO₄ solution (pH = 0) and 1.0 M KOH solution (pH = 14). f) Oxygen evolution Tafel plot of Pd-e-NiCo-PBA-C and the reference samples in 1.0 M KOH solution (pH = 14). g) Oxygen evolution polarization curves of Pd-e-NiCo-PBA-C in 0.5 M H₂SO₄ solution (pH = 0) (Inset: Tafel plot of Pd-e-NiCo-PBA-C). h) Hydrogen evolution and oxygen evolution polarization curves of Pd-e-NiCo-PBA-C before and after 5000 cycling tests. i) Overall water-splitting performances of Pd-e-NiCo-PBA-C||Pd-e-NiCo-PBA-C electrode couples and IrO₂||Pt/C electrode couples in 1 M KOH (Inset: Chronoamperometry test for Pd-e-NiCo-PBA-C||Pd-e-NiCo-PBA-C at an applied potential of 1.6 V in 1 M KOH). j,k) Comparison of hydrogen evolution properties with some recently reported high-performance catalysts in 0.5 M H₂SO₄ (pH = 0) and 1.0 M KOH solution (pH = 14). l) Comparison of oxygen evolution properties with some recently reported high-performance catalysts in 1.0 M KOH solution (pH = 14).

The extremely low overpotential of Pd-e-NiCo-PBA-C in both acidic and alkaline electrolyte (Figure 7g and Table S3, Supporting Information) and excellent stability indicate that it is a

competitive state-of-the-art HER catalyst. From the above observations, it is concluded that the excellent HER performance is mainly due to the conductive graphite carbon matrix, favorable

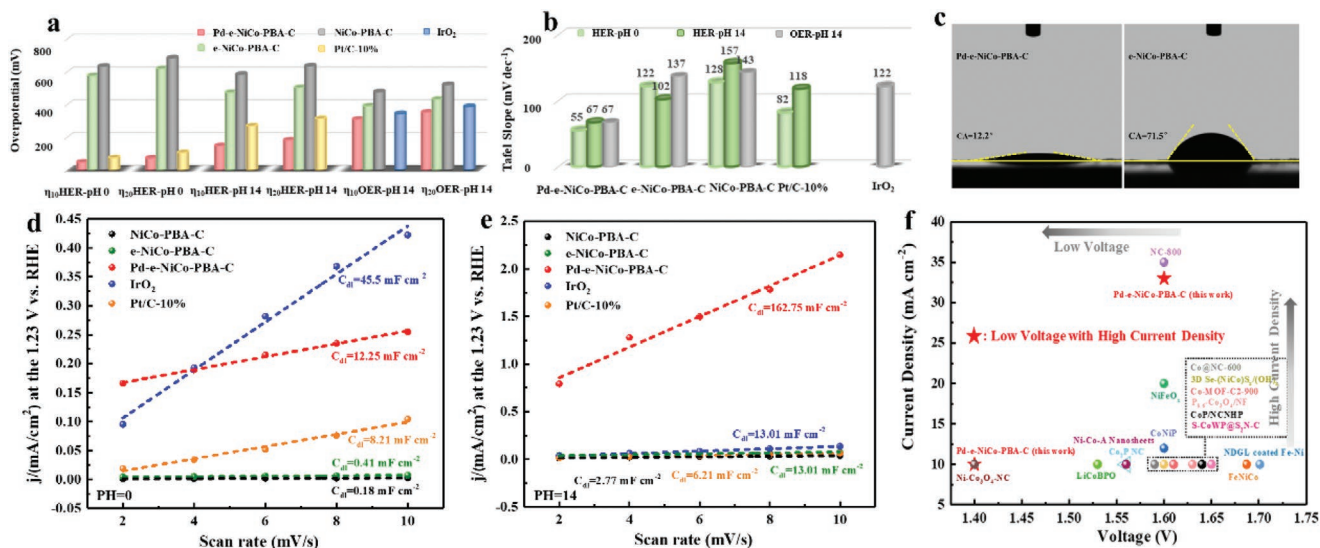


Figure 8. Electrochemical performance. a) The overpotentials comparison needed to deliver anodic current densities of 10 and 20 mA cm⁻² for Pd-e-NiCo-PBA-C and the reference samples for HER (pH = 0, pH = 14) and OER (pH = 14). b) Tafel Slopes comparison of Pd-e-NiCo-PBA-C and the reference samples for HER (pH = 0, pH = 14) and OER (pH = 14). c) Contact angles of Pd-e-NiCo-PBA-C and e-NiCo-PBA-C. d, e) Capacitive current measured at 1.23 V (vs RHE) of Pd-e-NiCo-PBA-C as a function of scan rate in 0.5 M H₂SO₄ solution (pH = 0) and 1.0 M KOH solution (pH = 14). f) Comparison of overall water-splitting properties with some recently reported high-performance catalysts in 1.0 M KOH solution (pH = 14).

electrolyte diffusion property, high specific surface area, and electronic configuration modulation with codoping of nitrogen and nickel, as well as the unique dodecagon nanosheet structure.

Furthermore, the OER performance of Pd-e-NiCo-PBA-C in O₂-saturated 1.0 M KOH solution was explored and compared with a series of products including NiCo-PBA-C, e-NiCo-PBA-C, commercial IrO₂, and GCE.

As shown in Figures 7c and 8a, under alkaline conditions, at current densities of 10 and 20 mA cm⁻², the overpotential of Pd-e-NiCo-PBA-C is only 309 mV ($\eta_{10\text{OER-alkaline}}$) and 352 mV ($\eta_{20\text{OER-alkaline}}$), much better than that of NiCo-PBA-C (476 mV- $\eta_{10\text{OER-alkaline}}$, 520 mV- $\eta_{20\text{OER-alkaline}}$), e-NiCo-PBA-C (390 mV- $\eta_{10\text{OER-alkaline}}$, 431 mV- $\eta_{20\text{OER-alkaline}}$), and even better than that of commercial IrO₂ (343 mV- $\eta_{10\text{OER-alkaline}}$, 386 mV- $\eta_{20\text{OER-alkaline}}$). The Tafel slope of Pd-e-NiCo-PBA-C has been calculated to be only 67 mV dec⁻¹, which implies that chemical adsorption of OH⁻ on the catalyst might limit the reaction rate. The Tafel slope (Figures 7f and 8b) of other reference samples of NiCo-PBA-C, e-NiCo-PBA-C, and commercial IrO₂ are 137, 143, and 122 mV dec⁻¹, respectively. It is obvious that the catalytic performance follows the same order as observed with HER, that is, Pd-e-NiCo-PBA-C > e-NiCo-PBA-C > NiCo-PBA-C.

Combined with XRD, SEM, and TEM analysis, it suggests that the better HER and OER performance of e-NiCo-PBA-C can be attributed to the higher degree of crystallinity and enhanced electrons and ions transportation supported with electrified graphite carbon substrate, as well as the unique nanostructure. Whereas the inferior performance of NiCo-PBA-C could be attributed to the amorphous carbon induced from incomplete carbonization or larger crystallite sizes of the electrochemically active components.

The results of multiple reproducibility tests exhibited good repeatability and stability with less than 5% variation

(Figure S16, Supporting Information). More importantly, OER performance is rarely reported in literature under acidic conditions due to the lack of hydroxyl and relative long electron transfer path, while Pd-e-NiCo-PBA-C showed excellent OER catalytic activity in 0.5 M H₂SO₄ electrolyte, comparable with the most state-of-the-art polyoxometalate acidic OER electrocatalysts.^[50] The overpotential of Pd-e-NiCo-PBA-C is only 290 mV, and the Tafel slope was calculated as 220 mV dec⁻¹ (Figure 7g). Moreover, the OER performance of Pd-e-NiCo-PBA-C in alkaline condition remained nearly unchanged after 5000 cycles of successive CV tests (Figure 7h), demonstrating the excellent stability. However, the OER catalytic stability of Pd-e-NiCo-PBA-C in acidic solution is not as good as others, after 500 cycles, the overpotential showed a relative large decrease of 20.7% at the current density of 10 mA cm⁻² (Figure S7, Supporting Information), owing to the corrosion of the catalysts at higher proton concentrations.

The above results and comparisons with other state-of-the-art electrocatalysts (Figure 7l and Table S5, Supporting Information) suggest that Pd-e-NiCo-PBA-C is a very effective OER catalyst, regardless of electrolyte pH. The high OER activities, especially in acidic solution, can be ascribed to the carbon conducting support with metallic composite which can improve the stability of electrocatalysts in acidic media by providing a relatively hydrophobic environment.^[50]

Due to the excellent HER and OER properties of the Pd-e-NiCo-PBA-C, it was used as a bifunctional catalyst for both the anode and cathode in a simple two-electrode system to study the overall water-splitting performance. As shown in Figure 7i, the current density of Pd-e-NiCo-PBA-C||Pd-e-NiCo-PBA-C is 33 mA cm⁻² at a cell voltage of 1.6 V, which is comparable with that of IrO₂||Pt/C couple (20 mA cm⁻² at 1.6 V). Compared with the comparisons with other high-performance overall water-splitting catalysts (Figure 8f and Table S6,

Supporting Information), Pd-e-NiCo-PBA-C||Pd-e-NiCo-PBA-C exhibits a high total current density and excellent full water hydrolysis performance. Furthermore, the stability of Pd-e-NiCo-PBA-C||Pd-e-NiCo-PBA-C was evaluated using constant chronoamperometry measurement (Figure 7i inset), after over 50 h of continuous overall water electrolysis; Pd-e-NiCo-PBA-C||Pd-e-NiCo-PBA-C remained stable and kept $\approx 97.3\%$ catalytic activity, demonstrating its remarkable durability.

Water contact angle tests (Figure 8c) were conducted to study wettability while being submerged, which is necessary for electrocatalytic testing in solution. Pd-e-NiCo-PBA-C displayed super-hydrophilic (water contact angle, 12.2°) properties, while e-NiCo-PBA-C showed hydrophobic (water contact angle, 71.5°) properties. Similarly, commercial Pt/C and IrO_2 also have hydrophilic performance, with literature reporting that the contact angles are larger than that of Pd-e-NiCo-PBA-C, 36.6° and 30.0° , respectively.^[58,59] This reveals the as-obtained catalysts, after selective etching and ion exchange, have a better wettability performance in water, resulting in full contact with the electrolyte and consequently better water-splitting performance.

To shed light on the low HER and OER overpotentials and high catalytic performance of Pd-e-NiCo-PBA-C, electrochemical surface area (ECSA) of the samples was calculated by the CV method. ECSA of materials is an important indicator of electrochemical activity, and it is directly proportional to the electrochemical double-layer capacitance (C_{dl}) in the non-Faradaic region, where charge transfer can be ignored due to electrode reaction and the current density is only from the charging and discharging of the electric double layer. According to the CV results, Figures S8 and S9, Supporting Information, the electrochemical double-layer capacitances of Pd-e-NiCo-PBA-C in acidic and alkaline solution were calculated and are shown in Figure 8d,e; they were 12.25 and $162.75 \text{ mF cm}^{-2}$, respectively. The values are much larger than that of NiCo-PBA-C ($0.18 \text{ mF cm}^{-2} \cdot C_{dl\text{-acidic}}$ and $13.01 \text{ mF cm}^{-2} \cdot C_{dl\text{-alkaline}}$) and e-NiCo-PBA-C ($0.41 \text{ mF cm}^{-2} \cdot C_{dl\text{-acidic}}$ and $2.77 \text{ mF cm}^{-2} \cdot C_{dl\text{-alkaline}}$), indicating Pd-e-NiCo-PBA-C has more active surface area than the other comparison samples. The C_{dl} of NiCo-PBA-C is smaller than that of e-NiCo-PBA-C, suggesting lower charge accumulation between the amorphous carbon and water interfaces.

EIS was also used to study the charge transfer resistance (R_{ct}) in these materials. By applying an AC voltage of 5 mV amplitude in a frequency range from 0.01 Hz to 100 kHz at open circuit potential, the obtained Nyquist plots and equivalent circuit are displayed in Figure S10, Supporting Information. In the equivalent circuit, R_s is the solution resistance, R_1 is the charge transfer resistance related to the electrocatalysis process, CPE1 (constant phase element) is related to the capacitance, W1 refers to Warburg resistance resulting from the diffusion in the electrode channels.^[58] The observed slope in the Nyquist plots of Pd-e-NiCo-PBA-C was smaller than those of NiCo-PBA-C and e-NiCo-PBA-C, suggesting rapid electron transport for water electrocatalysis within the electrode system. This could be attributed to the formation of highly conductive and electrochemically active metal that allows minimization of interface-resistance potentials, leading to an excellent electron transport pathway for water-splitting.

To investigate the relatively poor OER stability of Pd-e-NiCo-PBA-C in acidic solution, after 500 cycling test, it was

further characterized by XPS (Figure S11, Supporting Information). From the C 1s XPS spectrum, there is an extra peak of O-C=O after cycling, which indicates material oxidation during the process. Detailed analysis of Co 2p XPS spectra of the Pd-e-NiCo-PBA-C after the OER tests revealed that Co^{III} and Co^{IV} species were reduced to Co^{II} and Co^{III} species, and the relative content of surface Pd^{II} species increased, while that of metallic Pd decreased. These phenomena indicate the catalytic active sites, Co^{IV} and metallic Pd, in Pd-e-NiCo-PBA-C were inactive due to the strong acid solution and oxidation of O_2 .^[60,61] In addition, The N 1s XPS spectrum of Pd-e-NiCo-PBA-C displayed obvious decline before and after long-term stability tests, which is another evidence confirming the loss of active species.

These phenomena confirm the synergic catalytic effect of dodecagon nanosheet with metallic compound species in the graphite carbon matrix, resulting in a superior electrocatalyst for both OER and HER. In addition, the nitrogen-containing groups in the d-band electrons of metals and their oxides also make them more favorable for water splitting, allowing the rapid transport of electrons and substances, thereby promoting the breaking and formation of bonds during water splitting, further enhancing the electrocatalytic activity.

An economic analysis of Pd-e-NiCo-PBA-C was carried out (Figure S14, Supporting Information). A price comparison of Pd and Pt show that prior to January 2018, the price of Pd was lower than that of Pt, and thereafter the price of Pd was higher. In the price comparison of Pd and Ir, the price of Ir is mostly higher than that of Pd, only over brief periods is this reversed. The prices of Pd-e-NiCo-PBA-C, Pt/C-10%, and IrO_2 were compared from January 2014 to January 2020. Prior to June 2017, Pd-e-NiCo-PBA-C was cheaper than Pt/C-10%. For Pd-e-NiCo-PBA-C and IrO_2 , the price of Pd-e-NiCo-PBA-C has always been advantageous.

3.3. Theoretical Calculations and Simulations

In order to further understand the superior performance of the samples with Pd, theoretical calculations were carried out by DFT modeling. Two simplified models were built to simulate the experimentally synthesized systems. Pd-Co and Ni-Co were put on a continuous film of carbon, as illustrated in Figure 9a and Figure S12, Supporting Information. The optimized cell structure in Figure 9a indicates that the adsorption site is above the center of the metal atoms for both PdCo@C and NiCo@C. The free energy for HER is correlated to the adsorption energy between the surface of base material with H^* , and for OER, the free energy is related to intermediates of HO^* , O^* , and HOO^* . Free energy diagrams are plotted (Figure 9b,c) in both systems, suggesting the adsorption energies of the intermediate states with adsorbed gas atoms to reflect their performance in HER and OER. As is known, the catalyst with ΔG closer to zero indicates potentially better performance in electrocatalysis.^[62,63] The $\Delta G(\text{H}^*)$ is calculated to be -0.837 eV for PdCo@C and -1.010 eV for NiCo@C, which are in agreement with the experimental results. For OER, it can be found that the potential limiting step of both PdCo@C and NiCo@C for the reaction path was

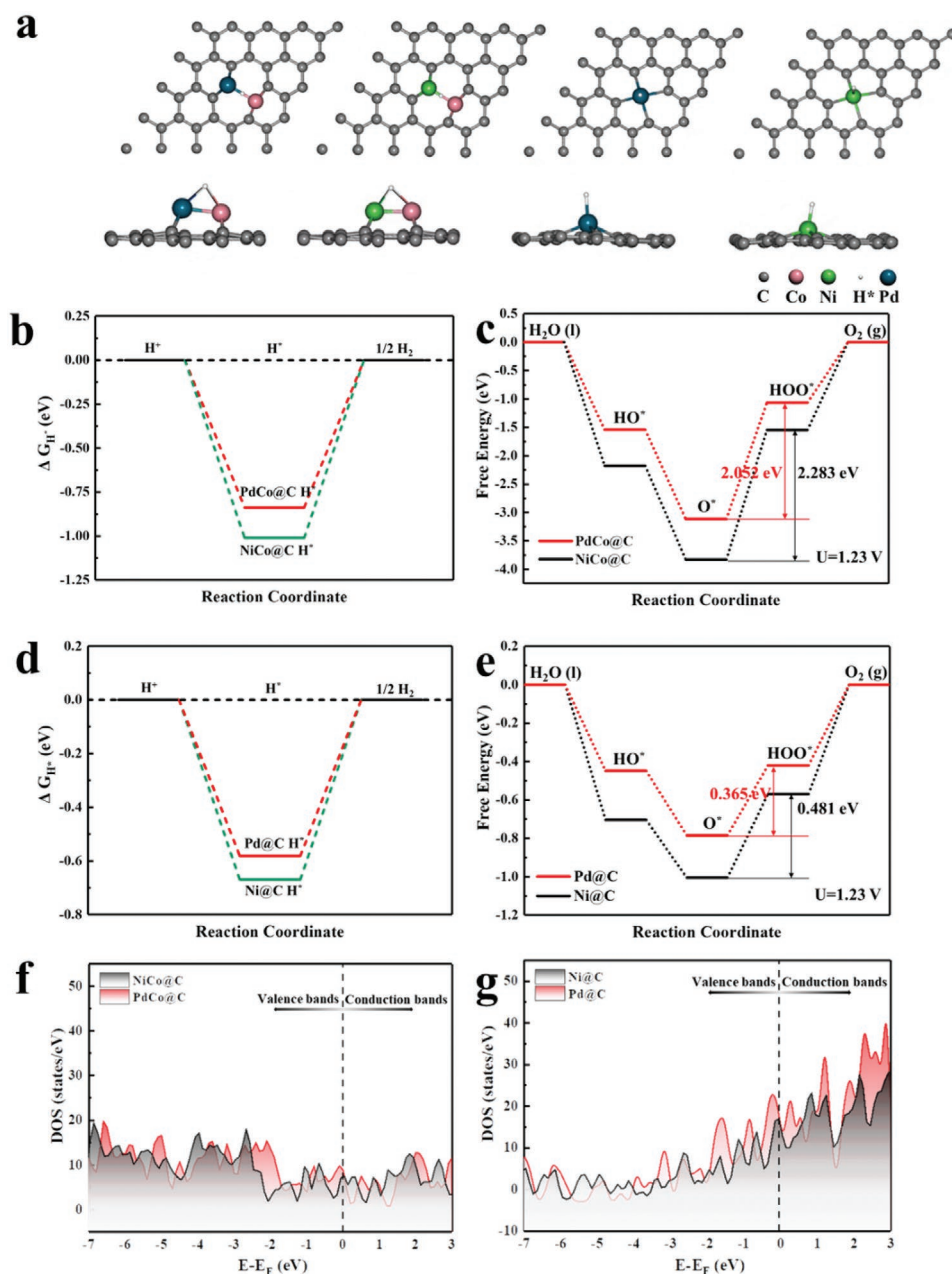


Figure 9. a) 3D schematic of DFT optimized geometric structures for PdCo@C-H*, NiCo@C-H*, Pd@C-H*, and Ni@C-H*. DFT modeled free energy diagram of b) HER and c) OER for PdCo@C and NiCo@C and d) HER and e) OER for Pd@C and Ni@C. Density of states spectra of f) NiCo@C (black) and PdCo@C (red) and g) Ni@C (black) and Pd@C (red), with Fermi energy normalized to 0.

the third proton–electron transfer steps of forming HOO* from O* (Figure 9c). After the replacement of the Ni with Pd in the models, the free energy value of the potential limiting step was lowered significantly, revealing a reduced energy barrier for formation of HOO*. The lower binding energy of HOO* with the PdCo bimetal pair is possibly due to the inertness of Pd. The modeled systems with single metal atoms show similar results as in diatomic models (Figure 9d,e). It is worth mentioning that the difference in free energy between the single-atom model and the diatomic model mainly lies in different binding sites. The binding site of the diatomic

model is located in the middle of the two atoms, which leads to a larger negative ΔG . Compared with the single-atom model, the diatomic model has better affinity for gas atoms and metal atoms.

The result of our DFT calculations provided two models for the simulation of the possible active sites in the nanoparticles. The simplification of the full crystal structure makes it clear to consider the conjunction sites of reaction intermediates with catalytic atoms. As a supportive method, the DFT calculation is based on the assumption that the catalytic performance is mainly determined by the metal–metal bridge site, which is

an approximation adopted in many theoretical works.^[64–67] The free energy results suggest the replacement of active atoms with inert atoms could decrease the binding energy between active atoms and intermediate species, which provide an insight to the improvement of electrocatalytic activity. Meanwhile, Figure 9f,g, and Figure S13, Supporting Information, show the calculated density of state and band structure for the modeled systems. Metallic properties can be expected in the modeled systems and no clear band gap can be seen in their band structure and DOS diagram.

4. Conclusion

In summary, a high performing bicatalyst was synthesized by the pyrolysis of a PBA; the composition and microstructure of the material were controlled by ion-exchange and anisotropic etching of the precursor. Detailed characterization indicates the final material consists of CoPd₂ on graphite planar dodecahedra. The results show that the novel dodecagon N-doped PdCoNi carbon-based nanosheets display outstanding catalytic performance and long-term stability on OER, HER, and overall water-splitting. Moreover, the preparation procedure can be adapted to produce a range of microstructured noble metal and alloy catalysts.

Supporting Information

Supporting Information is available from the Wiley Online Library or from the author.

Acknowledgements

H.Z. acknowledges the Imperial College London and China Scholarship Council (IC-CSC) and EPSRC Centre for Doctoral Training in the Advanced Characterization of Materials (EP/L015277/1). The authors acknowledge use of characterization facilities within the Harvey Flower Electron Microscopy Suite at the Department of Materials, Imperial College London.

Conflict of Interest

The authors declare no conflict of interest.

Keywords

cation-exchanges, CoPd₂, dodecagon nanosheets, overall water-splitting, Prussian blue analogues

Received: November 13, 2020
Published online: December 13, 2020

- [1] D. Sheberla, J. C. Bachman, J. S. Elias, C.-J. Sun, Y. S.-Horn, M. Dinc, *Nat. Mater.* **2017**, *16*, 220.
[2] X. Cao, C. Tan, M. Sindorob, H. Zhang, *Chem. Soc. Rev.* **2017**, *46*, 2660.

- [3] R. Wu, D. Wang, V. Kumar, K. Zhou, A. Law, P. Lee, J. Lou, Z. Chen, *Chem. Commun.* **2015**, *51*, 3109.
[4] L. Xie, R. Zhang, L. Cui, D. Liu, S. Hao, Y. Ma, G. Du, A. Asiri, X. Sun, *Angew. Chem., Int. Ed.* **2017**, *56*, 1064.
[5] L. Jiao, Y.-X. Zhou, H.-L. Jiang, *Chem. Sci.* **2016**, *7*, 1690.
[6] F. Ming, H. Liang, H. Shi, X. Xu, G. Mei, Z. Wang, *J. Mater. Chem. A* **2016**, *4*, 15148.
[7] X. Y. Yu, Y. Feng, Y. Jeon, B. Guan, X. W. Lou, U. Paik, *Adv. Mater.* **2016**, *28*, 9006.
[8] Y. Feng, X.-Y. Yu, U. Paik, *Chem. Commun.* **2016**, *52*, 6269.
[9] P. Chen, K. Xu, Z. Fang, Y. Tong, J. Wu, X. Lu, X. Peng, H. Ding, C. Wu, Y. Xie, *Angew. Chem., Int. Ed.* **2015**, *54*, 14710.
[10] S. Wang, J. Wang, M. Zhu, X. Bao, B. Xiao, D. Su, H. Li, Y. Wang, *J. Am. Chem. Soc.* **2015**, *137*, 15753.
[11] S. Dou, L. Tao, J. Huo, S. Wang, L. Dai, *Energy Environ. Sci.* **2016**, *9*, 1320.
[12] J. G. Chen, C. W. Jones, S. Linic, V. R. Stamenkovic, *ACS Catal.* **2017**, *7*, 6392.
[13] H. Hu, B. Guan, B. Xia, X. W. Lou, *J. Am. Chem. Soc.* **2015**, *137*, 5590.
[14] M. Cao, X. Wu, X. He, C. Hu, *Chem. Commun.* **2005**, *17*, 2241.
[15] X.-Y. Yu, L. Yu, H. B. Wu, X. W. Lou, *Angew. Chem., Int. Ed.* **2015**, *54*, 5331.
[16] C. Xuan, J. Wang, W. Xia, Z. Peng, Z. Wu, W. Lei, K. Xia, H. L. Xin, D. Wang, *ACS Appl. Mater. Interfaces* **2017**, *9*, 26134.
[17] A. Indra, U. Paik, T. Song, *Angew. Chem., Int. Ed.* **2017**, *57*, 1241.
[18] X.-Y. Yu, Y. Feng, B. Guan, X. W. Lou, U. Paik, *Energy Environ. Sci.* **2016**, *9*, 1246.
[19] J. Zhou, Y. Wang, X. Su, S. Gu, R. Liu, Y. Huang, S. Yan, J. Li, S. Zhang, *Energy Environ. Sci.* **2019**, *12*, 739.
[20] Q.-X. Chen, Y.-H. Liu, X.-Z. Qi, J.-W. Liu, H.-J. Jiang, J.-L. Wang, Z. He, X.-F. Ren, Z.-H. Hou, S.-H. Yu, *J. Am. Chem. Soc.* **2019**, *141*, 10729.
[21] H. Hu, B. Y. Guan, X. W. Lou, *Chem* **2016**, *1*, 102.
[22] W. Zhang, Y. Zhao, V. Malgras, Q. Ji, D. Jiang, R. Qi, K. Ariga, Y. Yamauchi, J. Liu, J.-S. Jiang, M. Hu, *Angew. Chem.* **2016**, *128*, 8368.
[23] J. Nai, Y. Lu, L. Yu, X. Wang, X. W. Lou, *Adv. Mater.* **2017**, *29*, 1703870.
[24] M. Hu, S. Furukawa, R. Ohtani, H. Sukegawa, Y. Nemoto, J. Reboul, S. Kitagawa, Y. Yamauchi, *Angew. Chem.* **2012**, *124*, 1008.
[25] L. Han, X.-Y. Yu, X. W. Lou, *Adv. Mater.* **2016**, *28*, 4601.
[26] L. Yu, H. B. Wu, X. W. Lou, *Acc. Chem. Res.* **2017**, *50*, 293.
[27] D. Su, M. Cortie, H. Fan, G. Wang, *Adv. Mater.* **2017**, *29*, 1700587.
[28] K. Qiu, G. Chai, C. Jiang, M. Ling, J. Tang, Z. Guo, *ACS Catal.* **2016**, *6*, 3558.
[29] X. Y. Ma, Y. Chen, H. Wang, Q. X. Li, W. F. Lin, W. B. Cai, *Chem. Commun.* **2018**, *54*, 2562.
[30] X. Li, Z. Lin, L. Yi, J. Lu, H. D. Abruña, *J. Am. Chem. Soc.* **2019**, *131*, 602.
[31] M. Shao, T. Yu, J. H. Odell, M. Jin, Y. Xia, *Chem. Commun.* **2011**, *47*, 6566.
[32] Y. Zuo, D. Rao, S. Li, T. Li, G. Zhu, S. Chen, L. Song, Y. Chai, H. Han, *Adv. Mater.* **2018**, *30*, 1704171.
[33] Y. Lu, Y. Jiang, X. Gao, X. Wang, W. Chen, *J. Am. Chem. Soc.* **2014**, *136*, 11687.
[34] B. Brandt, T. Schalow, M. Laurin, S. Schaueremann, J. Libuda, H. J. Freund, *J. Phys. Chem. C* **2007**, *111*, 938.
[35] Z. Xi, D. P. Erdosy, A. Mendoza-Garcia, P. N. Duchesne, J. Li, M. Muzzio, Q. Li, P. Zhang, S. Sun, *Nano Lett.* **2017**, *17*, 2727.
[36] B. S. Yeo, A. T. Bell, *J. Am. Chem. Soc.* **2011**, *133*, 5587.
[37] G. Mattioli, P. Giannozzi, A. Amore Bonapasta, L. Guidoni, *J. Am. Chem. Soc.* **2013**, *135*, 15353.
[38] P. Giannozzi, S. Baroni, N. Bonini, M. Calandra, R. Car, C. Cavazzoni, D. Ceresoli, G. L. Chiarotti, M. Cococcioni,

- I. Dabo, A. Dal Corso, S. Fabris, G. Fratesi, S. de Gironcoli, R. Gebauer, U. Gerstmann, C. Gougoussis, A. Kokalj, M. Lazzeri, L. Martin-Samos, N. Marzari, F. Mauri, R. Mazzarello, S. Paolini, A. Pasquarello, L. Paulatto, C. Sbraccia, S. Scandolo, G. Sclauzero, A. P. Seitsonen, A. Smogunov, P. Umari, R. M. Wentzcovitch, *J. Phys.: Condens. Matter* **2009**, *21*, 395502.
- [39] P. Giannozzi, O. Andreussi, T. Brumme, O. Bunau, M. B. Nardelli, M. Calandra, R. Car, C. Cavazzoni, D. Ceresoli, M. Cococcioni, N. Colonna, I. Carnimeo, A. D. Corso, S. de Gironcoli, P. Delugas, R. A. DiStasio Jr., A. Ferretti, A. Floris, G. Fratesi, G. Fugallo, R. Gebauer, U. Gerstmann, F. Giustino, T. Gorni, J. Jia, M. Kawamura, H.-Y. Ko, A. Kokalj, E. Küçükbenli, M. Lazzeri, M. Marsili, N. Marzari, F. Mauri, N. L. Nguyen, H.-V. Nguyen, A. Otero-de-la-Roza, L. Paulatto, S. Poncé, D. Rocca, R. Sabatini, B. Santra, M. Schlipf, A. P. Seitsonen, A. Smogunov, I. Timrov, T. Thonhauser, P. Umari, N. Vast, X. Wu, S. Baroni, *J. Phys.: Condens. Matter* **2017**, *29*, 465901.
- [40] G. Prandini, A. Marrazzo, I. E. Castelli, N. Mounet, N. Marzari, *npj Comput. Mater.* **2018**, *4*, 72.
- [41] M. Zhang, M. De Respini, H. Frei, *Nat. Chem.* **2014**, *6*, 362.
- [42] M. Favaro, J. Yang, S. Nappini, E. Magnano, F. M. Toma, E. J. Crumlin, J. Yano, I. D. Sharp, *J. Am. Chem. Soc.* **2017**, *139*, 8960.
- [43] E. Fabbri, M. Nachtegaal, T. Binniger, X. Cheng, B.-J. Kim, J. Durst, F. Bozza, T. Graule, R. Sch-ublin, L. Wiles, *Nat. Mater.* **2017**, *16*, 925.
- [44] H. Alamri, N. Ballot, J. Long, Y. Guari, J. Larionova, K. Kleinke, H. Kleinke, E. Prouzet, *Chem. Mater.* **2014**, *26*, 875.
- [45] M. Vondrova, T. M. McQueen, C. M. Burgess, D. M. Ho, A. B. Bocarsly, *J. Am. Chem. Soc.* **2008**, *130*, 5563.
- [46] J. Nai, Y. Lu, L. Yu, X. Wang, X. W. Lou, *Adv. Mater.* **2017**, *29*, 1703870.
- [47] M. Hu, J. S. Jiang, *Mater. Res. Bull.* **2011**, *46*, 702.
- [48] M. Vondrova, C. M. Burgess, A. B. Bocarsly, *Chem. Mater.* **2007**, *19*, 2203.
- [49] M. B. Stevens, L. J. Enman, A. S. Batchellor, M. R. Cosby, A. E. Vise, C. D. M. Trang, S. W. Boettcher, *Chem. Mater.* **2017**, *29*, 120.
- [50] M. Blasco-Ahicart, J. Soriano-López, J. J. Carbó, J. M. Poblet, J. R. Galan-Mascaros, *Nat. Chem.* **2018**, *10*, 24.
- [51] H. Furukawa, U. Mueller, O. M. Yaghi, *Angew. Chem., Int. Ed.* **2015**, *54*, 3417.
- [52] M. Hu, A. A. Belik, M. Imura, Y. Yamauchi, *J. Am. Chem. Soc.* **2013**, *135*, 384.
- [53] D. Yang, J. Xu, X.-Z. Liao, H. Wang, Y.-S. He, Z.-F. Ma, *Chem. Commun.* **2015**, *51*, 8181.
- [54] M. Celebi, M. Yurderi, A. Bulut, M. Kaya, M. Zahmakiran, *Appl. Catal., B* **2016**, *180*, 53.
- [55] Y. P. Zhu, T. Y. Ma, M. Jaroniec, S. Z. Qiao, *Angew. Chem., Int. Ed.* **2017**, *56*, 1324.
- [56] K. Fominykh, J. M. Feckl, J. Sicklinger, M. Doblinger, S. Bocklein, J. Ziegler, L. Peter, J. Rathousky, E. W. Scheidt, T. Bein, D. Fattakhova-Rohlfing, *Adv. Funct. Mater.* **2014**, *24*, 3123.
- [57] T. Ouyang, X. T. Wang, X. Q. Mai, A. N. Chen, Z. Y. Tang, Z. Q. Liu, *Angew. Chem., Int. Ed.* **2020**, *59*, 11948.
- [58] S. Anantharaj, P. E. Karthik, B. Subramanian, S. Kundu, *ACS Catal.* **2016**, *6*, 4660.
- [59] C. Chabanier, D. Guay, *J. Electroanal. Chem.* **2004**, *570*, 13.
- [60] Q. Wu, J. Xu, X. Yang, F. Lu, S. He, J. Yang, H. Fan, M. Wu, *Adv. Energy Mater.* **2015**, *5*, 1401756.
- [61] G. Zhao, K. Rui, S. X. Dou, W. Sun, *Adv. Funct. Mater.* **2018**, *28*, 1803291.
- [62] Q. W. Zhou, Z. H. Shen, C. Zhu, J. C. Li, Z. Y. Ding, P. Wang, F. Pan, Z. Y. Zhang, H. X. Ma, S. Y. Wang, H. G. Zhang, *Adv. Mater.* **2018**, *30*, 1800140.
- [63] J. Wang, F. Xu, H. Jin, Y. Chen, Y. Wang, *Adv. Mater.* **2017**, *29*, 1605838.
- [64] X. Zhao, X. Liu, B. Huang, P. Wang, Y. Pei, *J. Mater. Chem. A* **2019**, *7*, 24583.
- [65] Z.-P. Wu, B. Miao, E. Hopkins, K. Park, Y. Chen, H. Jiang, M. Zhang, C.-J. Zhong, L. Wang, *J. Phys. Chem. C* **2019**, *123*, 20853.
- [66] Z.-P. Wu, X. F. Lu, S.-Q. Zang, X. W. Lou, *Adv. Funct. Mater.* **2020**, *30*, 1910274.
- [67] I. C. Man, H. Y. Su, F. Calle-Vallejo, H. A. Hansen, J. I. Martínez, N. G. Inoglu, J. Kitchin, T. F. Jaramillo, J. K. Nørskov, J. Rossmeisl, *ChemCatChem* **2011**, *3*, 1159.